

Available online at www.sciencedirect.com**ScienceDirect**journal homepage: www.elsevier.com/locate/AJPS**Research Article**

CaCO₃-encircled hollow CuS nanovehicles to suppress cervical cancer through enhanced calcium overload-triggered mitochondria damage



Pengfei Wang ^{a,1}, Xichen Sun ^{a,1}, Liuyan Tang ^a, Ningning Li ^a, Qing Wang ^a, Bicheng Gan ^c, Yuezhou Zhang ^{a,b,*}

^a Xi'an Institute of Flexible Electronics (IFE) and Xi'an Institute of Biomedical Materials & Engineering (IBME), Northwestern Polytechnical University, Xi'an 710072, China

^b Ningbo Institute of Northwestern Polytechnical University, Frontiers Science Center for Flexible Electronics (FSCFE), Key laboratory of Flexible Electronics of Zhejiang Province, Ningbo 315103, China

^c College of Petroleum Engineering, Heilongjiang, Northeast Petroleum University, Daqing 163318, China

ARTICLE INFO**Article history:**

Received 13 May 2024

Revised 25 June 2024

Accepted 28 July 2024

Available online 2 November 2024

Keywords:

Hollow CuS nanovehicles

Tumor-specific synergistic therapy

Mitochondrial damage

Cascade-enhanced calcium

overload

ABSTRACT

Cervical cancer stands as a formidable malignancy that poses a significant threat to women's health. Calcium overload, a minimally invasive tumor treatment, aims to accumulate an excessive concentration of Ca²⁺ within mitochondria, triggering apoptosis. Copper sulfide (CuS) represents a photothermal mediator for tumor hyperthermia. However, relying solely on thermotherapy often proves insufficient in controlling tumor growth. Curcumin (CUR), an herbal compound with anti-cancer properties, inhibits the efflux of exogenous Ca²⁺ while promoting its excretion from the endoplasmic reticulum into the cytoplasm. To harness these therapeutic modalities, we have developed a nanoplateform that incorporates hollow CuS nanoparticles (NPs) adorned with multiple CaCO₃ particles and internally loaded with CUR. This nanocomposite exhibits high uptake and easy escape from lysosomes, along with the degradation of surrounding CaCO₃, provoking the generation of abundant exogenous Ca²⁺ *in situ*, ultimately damaging the mitochondria of diseased cells. Impressively, under laser excitation, the CuS NPs demonstrate a photothermal effect that accelerates the degradation of CaCO₃, synergistically enhancing the antitumor effect through photothermal therapy. Additionally, fluorescence imaging reveals the distribution of these nanovehicles *in vivo*, indicating their effective accumulation at the tumor site. This nanoplateform shows promising outcomes for tumor-targeting and the effective treatment in a murine model of cervical cancer, achieved through cascade enhancement of calcium overload-based dual therapy.

© 2024 Shenyang Pharmaceutical University. Published by Elsevier B.V.

This is an open access article under the CC BY-NC-ND license

(<http://creativecommons.org/licenses/by-nc-nd/4.0/>)

* Corresponding author.

E-mail address: iamyzzhang@nwpu.edu.cn (Y. Zhang).

¹ These authors contributed equally to this work.

Peer review under responsibility of Shenyang Pharmaceutical University.

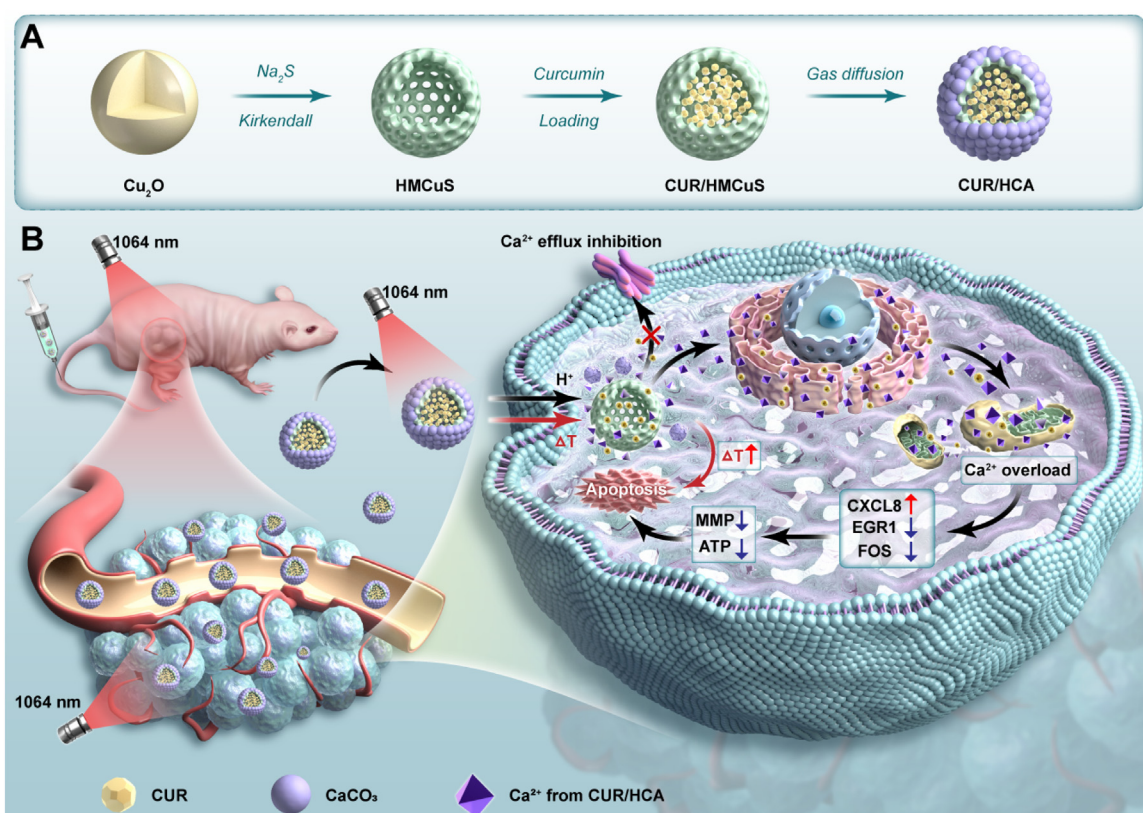
1. Introduction

Cancer poses a grave menace to human health and stands as the second most significant contributor to mortality rates globally [1,2]. Based on the World Health Organization's survey, it is predicted that 28.4 million novel cancer instances will emerge worldwide by 2040. Notably, several major economies will see cancer incidence and mortality rates rise to the forefront [3,4]. Cervical cancer, mainly caused by human papillomavirus infection, stands as one of the most common female malignancies [5]. Conventional therapeutic strategies come with severe toxic side effects and carry the risk of tumor metastasis [6]. Hence, there exists an imminent necessity to devise safer, smarter and more effective methods to combat cervical cancer. Mitochondria are not only the powerhouse that fuel cell functions [7], but also the key connectors between various signaling pathways pertaining to apoptosis, calcium homeostasis, and amino acid metabolism [8,9]. Targeting mitochondrial integrity and causing mitochondrial dysfunction have been proven as an efficacious strategy in inducing cell death [10–13]. This understanding paves the way for novel therapeutic approaches that specifically target mitochondria in the fight against cancer.

Inside mitochondria, both bound and free Ca^{2+} are present, working to maintain homeostasis [7,9]. However, a notable elevation in the amount of free Ca^{2+} can disrupt this balance, resulting in mitochondrial dysfunction and ultimately triggering cell apoptosis [14,15]. Manifestations of mitochondrial dysfunction include alterations in

morphology and structure, respiratory disorders, a reduction in mitochondrial membrane potential (MMP), decreased levels of adenosine triphosphate (ATP), and an overabundance of reactive oxygen species (ROS) generation [16–18]. Remarkably, cancer cells exhibit greater susceptibility to imbalances in Ca^{2+} homeostasis compared to normal ones [19]. This sensitivity is likely related to the specific Ca^{2+} signaling pathways and frequencies present in tumor cells [20,21]. Therefore, modulating the calcium concentration within mitochondria to induce apoptosis emerges as a potential cancer therapy approach. However, how to deliver free Ca^{2+} into cancer cells continuously and inhibit the efflux of Ca^{2+} remains unmet challenge [22].

Curcumin (CUR), a plant polyphenolic compound, is generally believed to inhibit cancer proliferation without significant side effects [23]. In tumor cells, CUR persistently stimulates the release of Ca^{2+} from the endoplasmic reticulum into the cytoplasm, thereby activating caspase channels and suppressing the expulsion of cytoplasmic Ca^{2+} via the plasma membrane; however, it remains inactive in normal cells [24]. However, CUR's poor solubility, instability, and low absorption rate limit its biomedical applications [25]. To address this, various calcium source have been explored for calcium overload-mediated tumor therapy, including calcium phosphate [26,27], calcium peroxide [28], and calcium carbonate [29]. Among them, calcium carbonate stands out due to natural abundance, low cost, good bioabsorbability, and biocompatibility. For example, Ding et al. developed a Ca^{2+} nanomodulator co-loaded with cisplatin and CUR, which



Scheme 1 – (A) Diagrammatic representation of the CUR/HCA preparation procedure. **(B)** Schematic diagram of the combined mechanism of CUR/HCA mediated synergistic enhancement of Ca^{2+} overload therapy.

effectively induced mitochondrial dysfunction in cancer therapy [29]. Additionally, they employed this nanomodulator as immunogenic cell death inducers, enhancing its effect when combined with ultrasound, effectively inhibiting tumor growth and metastasis [30]. Besides, this nanomodulator has shown the ability to induce pyroptosis [31]. Amorphous calcium carbonate (ACC), in particular, is highly hydrolyzed in the intracellular environment. Numerous studies have suggested the benefits of using ACC for drug delivery [32–35]. Given that combination therapies are often more effective in inhibiting tumor growth, the integration of CUR and ACC could be a beneficial strategy for calcium overload-induced cancer cell apoptosis. Besides, calcium overload frequently accompanies other treatment methods, including chemotherapy, photodynamic [36], photothermal therapy [37]. Notably, photothermal therapy can promote faster Ca^{2+} release, achieving synergistic therapeutic outcomes [38,39]. Copper sulfide, with its excellent photothermal conversion performance and low biotoxicity, is widely used in photothermal therapy [40]. Hollow mesoporous copper sulfide (HMCuS) offers additional advantages for drug loading and delivery, enhancing efficacy in combined therapy [41]. By co-loading calcium phosphate and CUR into HMCuS, the first near-infrared (NIR-I) photothermal enhanced calcium overload anti-cancer effect was achieved, further highlighting the material's advantages in drug loading and delivery for combined therapy [38]. Furthermore, compared to the NIR-I spectral range (spanning from 700 to 1,000 nm), and the secondary near-infrared (NIR-II) spectral range (covering 1,000 to 1,700 nm) allows for deeper tissue penetration [42].

Given these considerations, a nano-delivery system was devised that utilizes the benefits of the aforementioned elements to amplify the impact of calcium overloading, thereby realizing NIR-II guided multiple enhanced calcium overload anti-cancer effects. The resulting CUR/HMCuS@ CaCO_3 (CUR/HCA) nanoplatform exhibits several merits in facilitating dual therapy-based Ca^{2+} overload cancer therapy: first, it is easy to prepare and forms a structure that can universally load small molecule drugs; second, it can release CUR and Ca^{2+} in response to the tumor microenvironment (TME) and readily escape from lysosomes by consuming H^+ after being internalized; and most importantly, it enables cascade-boosted mitochondrial damage and apoptosis of cancer cells. Specifically, CUR/HCA is more favorably uptake by cancer cells compared to free CUR, leading to the accumulation of CUR and exogenous Ca^{2+} within the cells. Additionally, ACC undergoes selective and rapid degradation, resulting in a substantial release of exogenous Ca^{2+} in the TME, while CUR released from the hollow CuS inhibits the efflux of this Ca^{2+} . Furthermore, the photothermal properties of CUR/HCA accelerate ACC degradation, providing a boost for calcium overloading.

2. Material and methods

2.1. Material

Copper chloride dihydrate ($\text{CuCl}_2 \cdot 2\text{H}_2\text{O}$) was purchased from Macklin. Sodium chloride nonahydrate ($\text{NaCl} \cdot 9\text{H}_2\text{O}$),

Polyvinylpyrrolidone-K30 (PVP-K30), Ammonium bicarbonate (NH_4HCO_3), sodium dodecyl sulfate (SDS) and CUR were purchased from Adamas. Hydrazine hydrate ($\text{N}_2\text{H}_4 \cdot \text{H}_2\text{O}$) and Ethanol (EtOH) were purchased from Greagent. Calcium chloride dihydrate ($\text{CaCl}_2 \cdot 2\text{H}_2\text{O}$) was purchased from Damao Chemical Reagent Co., Ltd (Tianjin, China). Fluo-4AM, Rhod-2AM, and Mito-Tracker® Deep Red FM were purchased from Yeasen Biotechnology Co., Ltd (Shanghai, China). Lyso-Tracker® Red and JC-10 were purchased from Solarbio (Beijing, China). ATP testing kits was bought from Beyotime Institute of Biotechnology (Sichuan, China). HeLa cells was obtained from Shanghai Institute of Biochemistry and Cell Biology, Chinese Academy of Sciences (Shanghai, China). Dulbecco's modified Eagle's medium (DMEM), fetal bovine serum (FBS), hank's balanced salt solution (HBSS), trypsin-ethylenediaminetetraacetic acid solution, and penicillin-streptomycin liquid (penicillin: 10,000 U/ml, streptomycin: 10.0 mg/ml) were obtained from Jinbaoshun Biotechnology Co., Ltd. (Xi'an, China).

2.2. Synthesis of HMCuS

HMCuS were synthesized referring to the method reported by Ding et al. [43]. Here is a detailed description of the synthesis process: First, at room temperature, 200 μl $\text{CuCl}_2 \cdot 2\text{H}_2\text{O}$ (0.5 M) aqueous solution was mixed with 50 ml of 0.48 g PVP-K30 aqueous solution. After allowing the mixture to stir for 2 min, 50 ml pH 9 NaOH were added, succeeded by 8 μl hydrazine hydrate (80%, w/v) to obtain a suspension of bright yellow Cu_2O spheres. Following another 5 min of mixing, 400 μl Na_2S (1.33 M) aqueous solution was introduced to the suspension, and heated at a constant speed of 200 rpm at 60 °C for 2 h until the resulting solution was dark green. To purify the synthesized HMCuS, the resulting suspension was centrifuged at 11,000 rpm for 10 min. The NPs were then washed once with water and once with alcohol to eliminate any unreacted reagents or byproducts. Finally, the purified HMCuS NPs were dispersed in 5 ml ethanol and stored at room temperature for further use.

2.3. Synthesis of HMCuS@ CaCO_3 (HCA)

Magnetic stirring was performed at room temperature, slowly add the ethanol solution of HMCuS (5 ml, 5 mg/ml) into 50 ml $\text{CaCl}_2 \cdot 2\text{H}_2\text{O}$ ethanol solution (0.1 mg/ml). After stirring thoroughly for 5 min, transfer the above solution to a drying oven containing 5 g NH_4HCO_3 . The mixture was sealed and subjected to a reaction at 40 °C for 2 h, subsequently continuing the reaction at room temperature for an additional 12 h. Once the reaction was complete, the mixture was centrifuged at 9,000 rpm for 10 min to separate the solid product. The obtained HCA (HMCuS@ CaCO_3) was then dispersed in ethanol for storage at room temperature.

2.4. Synthesis of CUR/HCA

To prepare the CUR loaded nanocomposite, 10 mg CUR was added to an ethanol solution containing HMCuS nanoparticles (5 ml, 5 mg/ml) at room temperature. The mixture was stirred overnight in the dark to ensure thorough mixing. Following

this, the solution was centrifuged to separate the solid phase, which was then redispersed in 5 ml ethanol. Next, under magnetic stirring at room temperature, the ethanol solution of CUR/HMCuS (5 ml) was slowly added to 50 ml of a $\text{CaCl}_2 \cdot 2\text{H}_2\text{O}$ ethanol solution (0.1 mg/ml). After thorough mixing for 5 min, this solution was transferred to a drying oven containing 5 g NH_4HCO_3 . The mixture was then sealed and allowed to react at 40 °C for 2 h, followed by a further reaction at room temperature for 12 h. After the reaction was complete, the mixture was centrifuged at 9,000 rpm for 10 min to obtain the CUR loaded HMCuS@ CaCO_3 (CUR/HCA) nanocomposite. This nanocomposite was then dispersed in ethanol for storage at room temperature.

The loading capacity of CUR was calculated by the formula: Loading capacity (%) = $(M_{\text{CURtotal}} - M_{\text{CURfree}})/M_{\text{CUR/HCA}}$. Where M_{CURtotal} is the total CUR added into the ethanol solution of HMCuS, M_{CURfree} is the unloaded CUR in the supernatant, and $M_{\text{CUR/HCA}}$ refers to the total weight of prepared CUR/HCA.

Stability of CUR/HCA. The prepared CUR/HCA (200 µg/ml) was dispersed in PBS, DMEM and DMEM+FPS (10%) respectively, and its hydrated particle size was measured by Dynamic light scattering (DLS) every 2 d for 30 d

2.5. Ca^{2+} and CUR release of CUR/HCA

Acidity-triggered collapse of CUR/HCA. CUR/HCA (1 mg) was dispersed in PBS with 2% (w/v) SDS at pH 7.4, 6.4 and 5.4 for 12 h. Then, take different samples (10 µl) and drop them evenly on the carbon film and dry them for transmission electron microscopy (TEM) testing. TEM assessments were used to reveal the morphology changes of CUR/HCA at different pH values. **pH-responsive Ca^{2+} release from CUR/HCA.** CUR/HCA (10 mg) was dispersed in 1 ml HBSS with 2% (w/v) SDS at pH 5.4, 6.4 or 7.4, and then placed into a dialysis bag (molecular weight cut-off = 3,500 Da). Subsequently, the dialysis bag was immersed in 20 ml HBSS with the corresponding pH at 37 °C. At predetermined intervals, 1 ml external HBSS was collected and replaced with 1 ml of corresponding fresh HBSS. ICP-OES measured the amount of released Ca^{2+} . **pH-responsive CUR release from CUR/HCA.** CUR/HCA (10 mg) was dispersed in 1 ml of PBS with 2% (w/v) SDS at pH 5.4, 6.4 or 7.4, and then dispersed in 30 ml of PBS with the corresponding pH at 37 °C. At predetermined intervals, every sample was centrifuged to collect the supernatant, and another 1 ml corresponding fresh PBS was added. UV-Vis measured the amount of released CUR.

Photothermal promotes Ca^{2+} release. to assess the effect of Laser on Ca^{2+} release, CUR/HCA (10 mg) was dispersed in 10 ml PBS with 2% (w/v) SDS at pH 5.4, 6.4 or 7.4. CUR/HCA (1 mg/ml) was exposed to 1,064 nm laser (1 W/cm², 10 min) when dispersed in PBS solution (pH 6.4 and 5.4) for 20 min. The concentration of Ca^{2+} in the supernatant was determined by ICP-OES.

2.6. Photothermal effect of CUR/HCA

Under the excitation of a 1,064 nm laser (0.5 W/cm², 1 W/cm², 1.5 W/cm²; 10 min), the temperature and photothermal images of CUR/HCA in PBS (100, 200 and 300 µg/ml) were recorded at different times with a thermal imager.

The photothermal stability of the CUR/HCA was tested through three sets of cycles. Measure the temperature rise under laser irradiation for 10 min, turn off the laser and naturally cool to the initial temperature, and cycle three times.

The photothermal conversion efficiency can be calculated by Eq. 1:

$$\eta = \frac{hA(T_{\max} - T_{\text{sur}}) - Q_{\text{dis}}}{I(A - 10^{-A})} \quad (1)$$

Where T_{\max} represents the maximum steady-state temperature, T_{sur} denotes the surrounding ambient temperature, whereas Q_{dis} signifies the heat dissipation resulting from the absorption of light by both the solvent and the sample cell. hA was calculated according to Eq. 2:

$$\tau = \frac{M_D C_D}{hA} \quad (2)$$

Where M_D and C_D index the solution mass and heat capacity of pure water used as the solvent, respectively. As noted, τ can be calculated referring to the following Eq. 3:

$$t = \tau \ln \left(\frac{T_{\text{RT}} - T_{\text{sur}}}{T_{\max} - T_{\text{sur}}} \right) \quad (3)$$

Where T_{RT} denotes as the real-time temperature in the cooling period.

2.7. Cell uptake of CUR/HCA

Cells were plated into confocal Petri dishes at a concentration of 2×10^5 cells per well and incubated for 24 h to permit adequate adhesion and proliferation. Subsequently, the cells were rinsed with PBS and administered with CUR or CUR/HCA (CUR dosage: 20 µg/ml) for durations of 2 and 6 h, respectively. After treatment, the cells were washed twice with PBS to remove any unbound material. A confocal laser scanning microscope (CLSM, Nikon C2+&N-SIM E, Japan) was utilized to visually assess the cellular uptake of CUR when treated with the different materials. This allowed for a qualitative analysis of CUR's intracellular distribution. For a more quantitative analysis, flow cytometry (Beckman CytoFLEX, America) was employed. The cells were first detached using trypsin and then washed twice with PBS to eliminate any residual trypsin or media components. The cells were then resuspended in 0.2 ml PBS, prepared for flow cytometry analysis to quantitatively determine the extent of CUR uptake.

2.8. Lysosomal escape ability of CUR/HCA

Cells were plated onto confocal Petri dishes at a density of 2×10^5 cells per well and incubated for 24 h. Afterward, the cells were washed with PBS and exposed to CUR or CUR/HCA (CUR dose: 20 µg/ml) for 2 and 6 h, respectively. Following treatment, the cells were rinsed twice with PBS. Lysosomal staining was performed using the Lysotracker® Red probe. CLSM was used to visualize the degree of fluorescent colocalization of lysosomes and CUR.

2.9. Biodistribution of intracellular Ca^{2+} released by CUR/HCA in mitochondria

Cells were plated at a density of 2×10^5 cells per well in confocal Petri dishes and incubated for 24 h. Afterward, the cells were rinsed with PBS and then treated separately with PBS, CUR and CUR/HCA (CUR dosage: 20 $\mu\text{g}/\text{ml}$) for 4 h. Cells were subsequently washed twice with PBS. Mitochondria were stained using Mito-Tracker® Deep Red probe, while Fluo-4 probe was used to visualize Ca^{2+} . Visual characterization of mitochondria and Ca^{2+} fluorescent signals in different materials using CLSM.

2.10. Intracellular calcium overload

Cells were seeded in 6-well plate at the density of 2×10^5 cells per well and cultured for 24 h. Subsequently, cells were washed with PBS and treated with PBS, CUR, HCA, CUR/HCA, and CUR/HCA+Laser (CUR dose: 20 $\mu\text{g}/\text{ml}$; Ca^{2+} dose: 49.5 $\mu\text{g}/\text{ml}$) for 4 h, respectively. Cells were then washed with PBS twice. Rhod-2AM probe was utilized to stain Ca^{2+} . EVOS FL Auto Cell Imaging System (EVOS, Thermo Fisher EVOS FL Auto 2, America) was applied to visually characterize intracellular Ca^{2+} fluorescence signals after co-incubation with different materials.

2.11. Detection of MMP

Cells were seeded at 6-well plate at the density of 2×10^5 cells per well and cultured for 24 h. Subsequently, cells were washed with PBS and treated with PBS, CUR, HCA, CUR/HCA, and CUR/HCA+Laser (CUR dose: 20 $\mu\text{g}/\text{ml}$; Ca^{2+} dose: 49.5 $\mu\text{g}/\text{ml}$) for 6 h. Cells were then washed with PBS twice. JC-10 probe was utilized to stain mitochondria. CLSM was applied to visually characterize mitochondria membrane potential after co-incubation with different materials.

2.12. Measurement of intracellular ATP content

Cells were seeded in cell culture dish and treated with PBS, CUR, HCA, CUR/HCA and CUR/HCA + Laser (CUR dose: 20 $\mu\text{g}/\text{ml}$; Ca^{2+} dose: 49.5 $\mu\text{g}/\text{ml}$) for 6 h. After incubation, cells were lysed and centrifuged for 5 min at 12,000 g. The resulting supernatant was collected and used to measure intracellular ATP content according to the instructions of ATP testing kit.

2.13. In vitro cytotoxicity

Cells were seeded at 96-well plate at the density of 5×10^3 cells per well and cultured for 24 h. Subsequently, aspirate off the old medium and treated with different concentrations of HMCuS, HCA, CUR/HCA, and CUR/HCA+Laser for 24 h. Aspirate the medium and stain with Alamar blue in the dark for 4 h. A Microplate reader (TECAN Spark, Switzerland) was applied to measure cell viability after treatment with different materials.

2.14. RNA sequencing

HeLa cells were initially seeded in a 100 mm \times 20 mm dish at a density of 3.0×10^6 cells per dish in 8 ml DMEM

and cultured for 24 h. Following this incubation period, the medium was then treated with PBS, CUR, HCA, CUR/HCA and CUR/HCA+Laser (CUR dose: 20 $\mu\text{g}/\text{ml}$; Ca^{2+} dose: 49.5 $\mu\text{g}/\text{ml}$) for 10 h. After the washing with PBS twice, the cells were collected by using cell scraper and centrifuged to collect the precipitation for RNA sequencing.

2.15. In vivo biodistribution of IR820/HCA

Tumor-bearing mice were randomly divided into two groups and administered with IR820 and IR820-labeled HCA, respectively. Tracking the biodistribution of IR820 in mice using a small animal imaging system (IVIS Lumina Series III, America). Then major tissues (heart, liver, spleen, lung, kidney, and tumor) were removed at 48 h post injection. The synthesis of IR820/HCA was carried out according to the procedure outlined below. Briefly, IR820 (1 mg) and HCA (1 mg) were combined in 2 ml deionized water and sonicated for a duration of 2 h. Following the interaction, any unbound IR820 was separated by centrifugation and rinsed twice with deionized water.

2.16. In vivo photothermal effect of CUR/HCA

Tumor-bearing mice were randomly divided into two groups and administered with PBS or CUR/HCA (0.2 ml, CUR dose: 20 mg/kg). After tail vein injection for 12 h, the tumor site was irradiated with a 1,064 nm laser (1 W/cm²), and the temperature and images at different times were recorded with a thermal imager.

2.17. In vivo antitumor assays

Tumor-bearing mice were randomly divided into five groups ($n = 5$) and administered with (1) PBS, (2) CUR, (3) HCA, (4) CUR/HCA, and (5) CUR/HCA+Laser. PBS and different materials (CUR dose: 20 mg/kg; Ca^{2+} dose: 49.5 mg/ml) were injected into the tail vein on the 1st, 3rd, and 5th days, respectively, and observed for two weeks. For the NIR treated groups, after injection for 12 h, the tumor site was irradiated by 1064 nm laser (1 W/cm², 10 min). During the course of treatment, the tumor volume was quantified using a caliper and computed using the equation: tumor volume (mm³) = tumor length \times tumor width²/2. Additionally, throughout the treatment period, the body weight and survival status of all mice were documented. Upon completion of the treatment, various tissues (including heart, liver, spleen, lung, kidney, and tumor) were collected for histological staining with hematoxylin and eosin (H&E). Tumor tissues were further processed for TUNEL (terminal deoxynucleotidyl transferase-mediated dUTP nick end labeling) staining.

3. Results and discussion

3.1. Synthesis and characterization of CUR/HCA

The nanovehicles following the route outlined in Scheme 1 have been synthesized. Cu₂O NPs were generated by using CuCl₂ \cdot 2H₂O as the copper source, NaOH serves as a

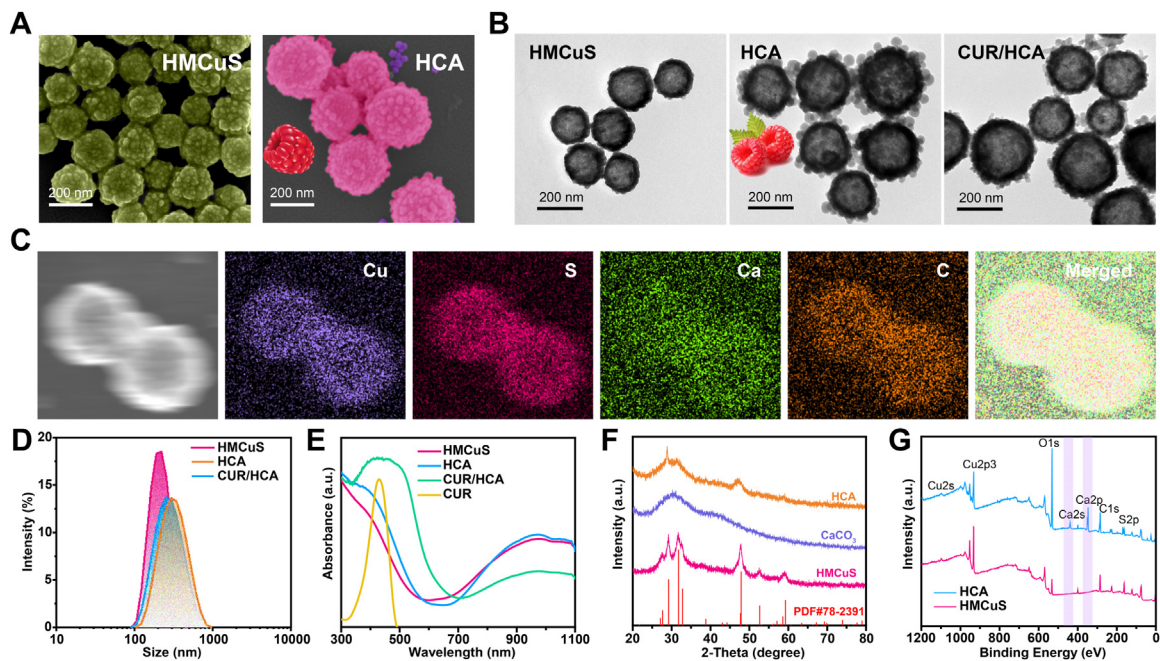


Fig. 1 – Characterizations of calcium-based nanovehicles. (A) SEM micro-images of HMCuS and HCA. **(B)** TEM micro-images of HMCuS, HCA and CUR/HCA. **(C)** Element mappings of CUR/HCA. **(D)** UV-vis-NIR absorption spectra, **(E)** Hydrodynamic diameters, and **(F)** X-ray diffraction pattern of HMCuS, HCA and CUR/HCA. **(G)** XPS full-spectrum of HMCuS and HCA.

pH regulator, N₂H₄·H₂O functions as a reductant, and PVP-K30 is utilized as a cross-linker. Due to the Kirkendall effect, the surface of Cu₂O is rapidly sulfated by Na₂S, leading to the formation of HMCuS. Afterwards, HMCuS was loaded with CUR. Lastly, CaCO₃ was generated *in situ* on the surfaces of HMCuS, serving as both a biocompatible reagent and a gatekeeper. The nitrogen adsorption-desorption curves and pore size distribution diagrams show that the specific surface area of HMCuS is 6.5358 m²/g, and the average pore diameter is 11.2 nm (Fig. S1A). These findings indicate the mesoporous nature of HMCuS, which is crucial for efficient drug loading and release.

To verify the successful synthesis of CUR/HCA, scanning electron microscopy (SEM) and TEM were utilized to visually inspect the material's morphology. As shown in Fig. 1A, HMCuS features a rough surface, providing a high specific surface area, clearly showing the successful adsorption of CaCO₃ NPs on its surface. Fig. 1B demonstrates the hollow and mesoporous structure of HMCuS with a diameter of approximately 200 nm, whereas HCA measures around 260 nm with a significant accumulation of CaCO₃ NPs. The presence of morphologically inhomogeneous agglomerates in CUR/HCA compared to HCA indicates the successful loading of CUR into HCA. The preparation of CUR/HCA was further confirmed by analytical techniques. Elemental mapping images (Fig. 1C) confirmed the existence of calcium, Raman spectra (Fig. S1B) showed characteristic signals at 1046 cm⁻¹ and 1087 cm⁻¹ corresponding to ν_{C-O} of CUR and CaCO₃, and UV-vis-NIR absorption spectra (Fig. 1E) revealed a CUR peak at 427 nm. Additionally, the loading capacity of CUR in CUR/HCA was determined to be 8.53 wt% based on UV-Vis absorption spectra (Fig. S1C). DLS measurements (Fig. 1D) indicated that

the hydration kinetic diameters of HMCuS, HCA and CUR/HCA were approximately 200, 270 and 250 nm, respectively. The shift in ζ potential observed in HCA and CUR/HCA compared to HMCuS provides evidence of successful CaCO₃ loading, as illustrated in Fig. S1D. The ζ potential of HMCuS measures at -18.7 mV, reflecting the alkaline conditions employed during its synthesis. Once the positively charged CaCO₃ is uniformly coated, HCA demonstrates a ζ potential of 25.78 mV. Furthermore, the ζ potential decreased from 25.78 to 5.31 mV, indicating the encapsulation of negatively charged CUR molecules within the HMCuS cavity.

The photothermal effect of HMCuS is due to its strong absorption in the NIR region and the surface plasmon resonance effect. As shown in Fig. 1E, HMCuS exhibits significant absorption in both NIR I and NIR II ranges, reaching a maximum absorption peak at approximately 1,083 nm. Similarly, HCA also shows robust absorption in these NIR regions, indicating comparable photothermal capabilities. Fig. 1F reveals that the diffraction pattern of HMCuS nanostructures aligns with hexagonal CuS (PDF #78-2391). The primary diffraction peaks located at 27.6°, 29.2°, 31.8°, 32.8°, 47.9°, 52.7°, and 59.3° correspond to the (101), (102), (103), (006), (110), (108) and (116) planes, respectively. Furthermore, X-ray diffraction patterns confirm that the CaCO₃ NPs adsorbed onto the surface of HMCuS are amorphous. Compared to CCC, ACC degrades more rapidly in the TME, releasing substantial amounts of exogenous Ca²⁺, thus offering the potential for calcium overload.

X-ray photoelectron spectroscopy (XPS) full-spectrum data reveals that HCA exhibits a prominent Ca2p orbital peak in contrast to HMCuS, suggesting the successful coating of ACC on the surface of HMCuS (Fig. 1G). Specifically, the peaks

observed in Ca 2p at binding energies of 350.48 and 346.98 eV correspond to Ca 2p1/2 and Ca 2p3/2, respectively, indicating the presence of CaCO_3 . As for Cu and S elements, peaks at binding energies of 952.30, 932.31 and 162.01 eV are assigned to Cu 2p1/2, Cu 2p3/2, and S-Cu, respectively, signifying the existence of CuS (Fig. S2). Additionally, to assess the stability of CUR/HCA, we simulated a plasma environment using DMEM supplemented with 10% FPS and tested its stability. As illustrated in Fig. S3, the hydrated particle size of CUR/HCA remains relatively unchanged in PBS, DMEM, and DMEM+FPS (10%), demonstrating its ability to function effectively in a normal physiological environment.

3.2. Mechanism of CaCO_3 formation on the surface of HMCuS

To explore why CaCO_3 precipitates as spherical NPs on the surface of HMCuS rather than forming a uniform coating, TEM images (Fig. 2A) of samples at various reaction intervals were collected. After a 40-min reaction, it became apparent that the surface of HMCuS was covered by a layer of CaCO_3 , creating a distinct core-shell structure. Subsequently, NPs started to emerge on the exterior of this CaCO_3 shell. Following a two-hour reaction, the CaCO_3 NPs were evenly spread across the surface of HMCuS. As the reaction progressed, these NPs continued to grow in size, leading to a gradual increase in system disorder. Based on these observations, we hypothesize that the uneven surface of HMCuS provides favorable nucleation sites for CaCO_3 growth, favoring the formation of a core-shell structure. Initially, core-shell NPs were observed to form, and subsequently, driven by interfacial energy, CaCO_3 tended to adopt the lowest-energy circular NP morphology. Consequently, with increasing reaction time, the CaCO_3 shells seemed to expand outwardly, culminating in the formation of circular NPs with the lowest energy configuration. The most symmetrical CaCO_3 decorated structure was evident when the reaction reached a two-hour mark. Additionally, Fig. S4 illustrates the hydrated particle size and polydispersity index curves of HCA at various reaction times.

Molecular dynamics (MD) simulations have become increasingly prevalent to unravel the kinetic mechanisms underlying various reactions [44]. To further understand the growth process of CaCO_3 on CuS surfaces, MD were employed to simulate, as represented in Fig. S5A. Due to electrostatic adsorption, Ca^{2+} and CO_3^{2-} ions spontaneously aggregated to form CaCO_3 particles, which then adhered to the CuS plate or spherical model (Fig. 2B and 2C). Our simulation showed a similar trend in both the planar and spherical models: an initial steep surge in total kinetic energy within the first 25 ps, which was followed by a precipitous decline. As the system equilibrated over the next 150 ps, the total kinetic energy gradually leveled off, stabilizing at ~280 kcal/mol for the planar model and 2,760 kcal/mol for the spherical model (Fig. 2D and 2E). The initial burst in kinetic energy can be explained by the mutual attraction and aggregation of Ca^{2+} and CO_3^{2-} ions within the simulated vacuum environment, which contributes significantly to the kinetic energy spike during their aggregation. However, as these ions adsorb onto the CuS surface, their kinetic energies decrease, resulting in the stabilization of the overall system's kinetic energy.

Additionally, it's worth mentioning that both potential energy and electrostatic energy exhibited a pattern of gradual decrease and stabilization over time (Fig. S5B and S5C).

As Ca^{2+} and CO_3^{2-} ions approached the surface of CuS, the intermolecular forces within the CuS planar model increased from 1,500 to approximately 3,400 kcal/mol. Conversely, when these ions adsorb to the surface of the spherical CuS model, intermolecular forces decreased from ~46,000 to ~40,000 kcal/mol (Fig. 2F). This observation implies that the attractive interaction between Ca^{2+} and CO_3^{2-} ions progressively strengthened within the CuS planar model. However, in the spherical CuS model, the intermolecular forces between Ca^{2+} and CO_3^{2-} ions gradually weakened. Nonetheless, the intermolecular forces were significantly greater in the spherical model compared to the flat model, indicating that the spherical model of CuS was more conducive to attracting CaCO_3 particles, ultimately leading to the formation of a unique, clustered structure resembling a collection of spheres.

3.3. Photothermal effect of CUR/HCA

Based on UV-vis-NIR results, both CUR/HCA and HMCuS exhibit comparable absorption in the NIR region, implying that CUR/HCA might possess remarkable photothermal conversion properties. As illustrated in Fig. 3A, at a concentration of 200 $\mu\text{g/ml}$, CUR/HCA's temperature rises by 55.2 °C in just 10 min, whereas the control group's temperature increases by only 39.5 °C. This significant temperature difference underscores CUR/HCA's superior photothermal performance. Furthermore, as the concentration of CUR/HCA and the laser power increase, the maximum attainable temperature also rises (Fig. 3B). Fig. 3C shows thermal images captured during laser irradiation at various time intervals. Remarkably, under three consecutive irradiations, there was minimal variation in the peak temperature achieved by CUR/HCA, highlighting its remarkable photothermal stability (Fig. S6A). By applying a linear time conversion to the cooling phase $\ln\theta$ in Fig. S6B, we determined the system's heat transfer time constant to be 92.3. Utilizing Eq. 1, we calculated the photothermal conversion efficiency of CUR/HCA to be 25.7%.

3.4. Ca^{2+} and CUR release of CUR/HCA

Due to the pH sensitivity of amorphous ACC, the CUR loaded in CUR/HCA can be selectively released in the TME. Additionally, the dissociation of ACC generates Ca^{2+} , which is beneficial for inducing calcium overload, ultimately leading to the death of tumor cells. Initially, we investigated the release of CUR at various pH values and observed a deeper yellow color in the PBS supernatant at pH 5.4, indicating higher CUR release under acidic conditions (Fig. S6C). Subsequently, TEM images taken at various pH levels further supported the increased dissociation of CaCO_3 at lower pH values. TEM characterization was performed to visualize the morphological changes of CUR/HCA after treatment with solutions of different pH. As depicted in Fig. S6D-F, the NPs remained stable at pH 7.4, while some CaCO_3 NPs began to dissociate at pH 6.4. Notably, almost all CaCO_3 NPs dissociated at pH 5.4, and HMCuS showed signs of

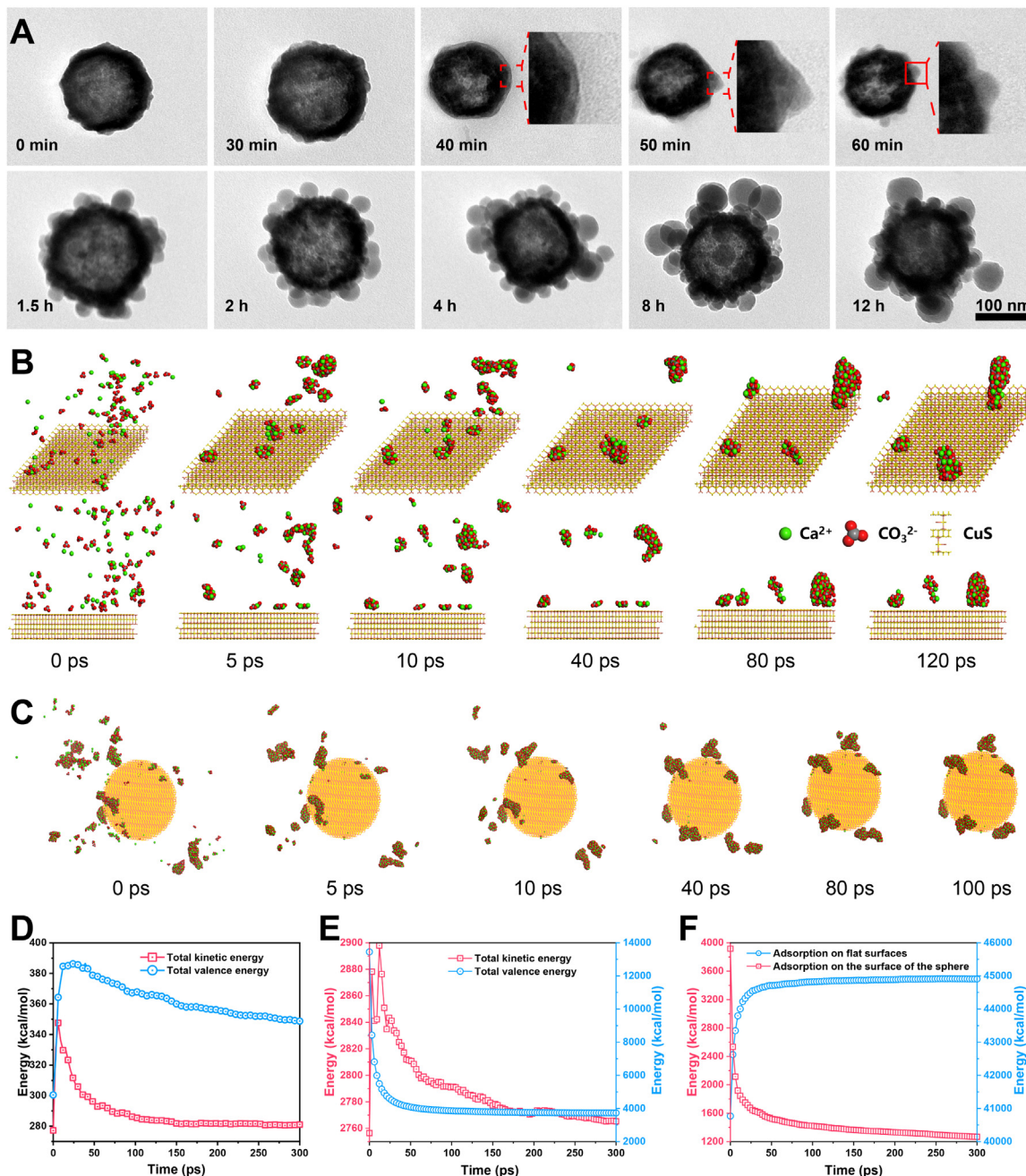


Fig. 2 – TEM images and MDs simulations during the formation process of HCA. (A) TEM images of HCA obtained at different reaction times. **(B)** The aggregation process of Ca^{2+} and CO_3^{2-} on the CuS plate model at different time points. **(C)** The aggregation process of Ca^{2+} and CO_3^{2-} on the CuS spherical model at different time points. **(D)** Kinetic and valence energy changes of the system during agglomeration of Ca^{2+} and CO_3^{2-} on the surface of a CuS plate model. **(E)** Kinetic and valence energy changes of the system during agglomeration of Ca^{2+} and CO_3^{2-} on the surface of a CuS spherical model. **(F)** Changes in intermolecular forces during agglomeration of Ca^{2+} and CO_3^{2-} on planar and spherical surfaces of CuS.

disintegration. These findings collectively establish the pH-responsiveness of CUR/HCA.

Considering the slightly acidic environment of tumors, we believe that our NPs exhibit specific drug release capabilities. The corresponding CUR and Ca^{2+} release curves further corroborate this conclusion (Fig. 3D and 3E). The release of Ca^{2+} reaches its peak within 1 hour, with maximum release

values of 86.03%, 63.94% and 37.25% at pH 5.4, 6.4 and 7.4, respectively. In contrast, CUR release peaks at 12 h due to its location within the HMCuS cavity, resulting in delayed release even as CaCO_3 degrades rapidly. The maximum CUR release was 81.56%, 52.68% and 41.46% at pH 5.4, 6.4 and 7.4, respectively. Importantly, we observed that laser irradiation significantly accelerates the release of Ca^{2+} , demonstrating

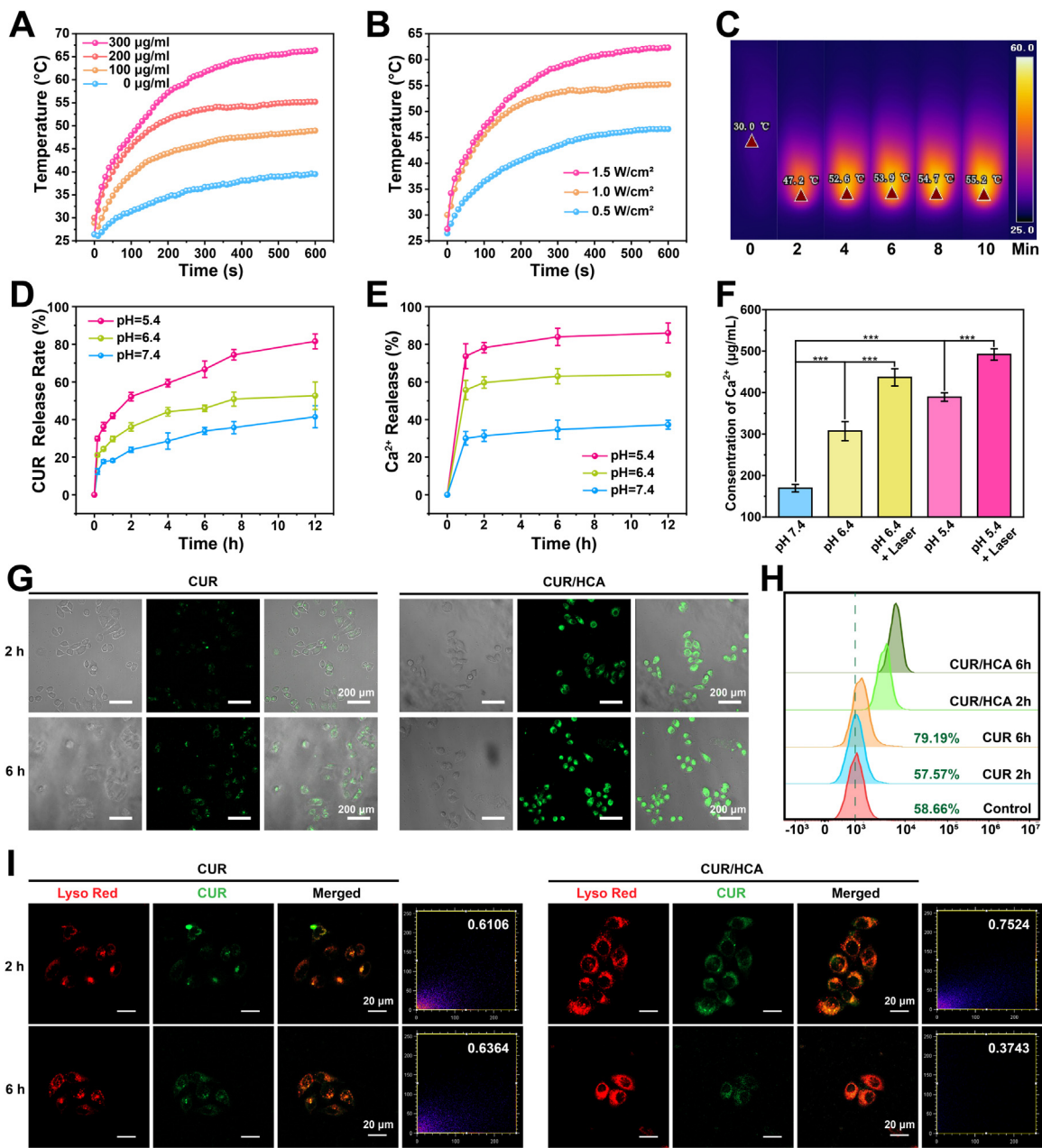


Fig. 3 – Photothermal, release effect, cellular uptake, and lysosomal escape of CUR/HCA. (A) Photothermal heating curve of CUR/HCA with irradiation by 1064 nm laser ($1 \text{ W}/\text{cm}^2$). (B) Photothermal heating curves of CUR/HCA under 1,064 nm laser irradiation with different powers. (C) Thermal images of CUR/HCA with irradiation by 1064 nm laser ($200 \mu\text{g}/\text{ml}$, $1 \text{ W}/\text{cm}^2$) for different time. (D) CUR release curves of CUR/HCA at different pH ($n = 3$). (E) Ca^{2+} release curves of CUR/HCA at different pH ($n = 3$). (F) The effect of pH and Laser on release of Ca^{2+} from CUR/HCA ($n = 3$). (G) CLSM micro-images of HeLa cells treated with CUR or CUR/HCA for 2 h or 6 h (green: CUR; Scale bar: $200 \mu\text{m}$). (H) Quantitative analysis of fluorescence intensity in HeLa cells from flow cytometry assays. (I) CLSM micro-images and colocalization analysis of HeLa cells treated with CUR or CUR/HCA for 2 h or 6 h (red: lysosome, green: CUR. Scale bar: $20 \mu\text{m}$).

that photothermal effects can promote the disintegration of CUR/HCA (Fig. 3F).

3.5. Intracellular uptake of CUR

Considering that CUR fluoresces when activated by a laser, this property enables the tracking of CUR distribution

within cells. As illustrated in Fig. 3G, within 2 h of co-incubating cells with CUR or CUR/HCA, the fluorescence emitted by CUR became evident in the cells, indicating effective CUR uptake. However, due to CUR's poor water solubility, the CUR-only group exhibited weaker fluorescence compared to the CUR/HCA group. When the co-incubation time was extended to 6 h, a higher fluorescence intensity

was observed in the cells, suggesting increased CUR uptake. These observations were further supported by flow cytometry data. Specifically, the fluorescence intensity of the CUR/HCA group was significantly stronger than that of the CUR-only group. Moreover, the fluorescence intensity after 6 h co-incubation was notably stronger than that after 2 h (Fig. 3H).

3.6. Lysosomal escape of CUR/HCA

Exogenous substances, upon entering cells, are typically sequestered by lysosomes initially. Given that NPs are prone to degradation in the acidic lysosomal environment, it's crucial to investigate whether CUR/HCA can avoid lysosomal entrapment. To explore this, lysosomes were stained with the Lyso-Tracker Red probe, and the biodistribution of both free CUR and CUR/HCA was observed using CLSM. By analyzing the colocalization of CUR fluorescence with the lysosomal stain, it was found that cells incubated with free CUR showed a consistently high degree of colocalization with lysosomes over time. In contrast, cells treated with CUR/HCA for 6 h exhibited a significant reduction in colocalization, suggesting that CUR/HCA can effectively evade lysosomal sequestration. This evasion might be attributed to the disintegration of ACC in acidic environments. As ACC breaks down, it consumes a large amount of protons (H^+), which can disrupt the lysosomal membrane, allowing CUR/HCA to escape the lysosome [38].

3.7. Ca^{2+} generation in cells

As previously established, amorphous ACC dissociates more readily in an acidic environment, releasing Ca^{2+} ions at a faster rate. To visualize the intracellular distribution of Ca^{2+} , we used Rhod-2, a cell-permeable calcium fluorescent probe, to capture intracellular Ca^{2+} levels. As shown in Fig. 4A, cells that were co-incubated with CUR/HCA exhibited the highest fluorescence intensity compared to other treatment groups. This finding suggests that the dissociation of ACC within the cells released a significant amount of Ca^{2+} , leading to elevated intracellular Ca^{2+} levels. The potential for Ca^{2+} overload is indicated by the strong fluorescence observed in these cells. The quantitative fluorescence intensity results obtained through flow cytometry were consistent with the qualitative observations made using EVOS imaging. Specifically, the CUR/HCA-treated cells demonstrated the highest fluorescence intensity (Fig. 4B), further supporting the occurrence of intracellular Ca^{2+} overload. Importantly, there were no significant differences in fluorescence intensity among the other treatment groups, emphasizing that it is the simultaneous delivery of CUR and a substantial amount of Ca^{2+} that leads to intracellular Ca^{2+} overload. This finding suggests a potential role for CUR/HCA in modulating intracellular Ca^{2+} levels, which may have implications for its therapeutic efficacy.

3.8. Mitochondrial damage caused by calcium overload

To further confirm that the Ca^{2+} released by CUR/HCA disintegration causes intracellular mitochondrial calcium

overload, we employed CLSM to visualize the distribution of calcium ions within mitochondria. We used the Mito Red probe to label mitochondria and the Fluo-4AM probe to capture intracellular Ca^{2+} . In comparison to the control and CUR-only groups, the CUR/HCA-treated group exhibited a stronger green fluorescence signal from the Fluo-4AM probe, indicating higher calcium levels. Additionally, there was a significant overlap between the green fluorescence from calcium and the red fluorescence from mitochondria, suggesting that CUR/HCA can indeed induce calcium overload specifically within mitochondria, potentially leading to apoptosis (Fig. S7).

To obtain a deeper understanding of mitochondrial damage, we used the Mito Deep Red probe, which emits red fluorescence, to study mitochondrial distribution within cells. Across all experimental groups, a noticeable decrease in both the distribution and intensity of red fluorescence were observed, indicating mitochondrial damage. Cells treated with CUR/HCA and exposed to laser light showed the lowest level of red fluorescence, indicating the most severe mitochondrial damage. These observations are consistent with the flow cytometry results presented in Fig. S8.

To validate the functional quality of mitochondria, the mitochondrial MMP using the JC-10 probe were assessed. A higher MMP indicates that mitochondria are producing more energy, reflecting intact mitochondrial function. When the MMP is high, the JC-10 probe forms aggregates that emit red fluorescence. In contrast, a low MMP causes the probe to exist primarily as monomers emitting green fluorescence. As shown in Fig. 4C, the control group exhibited the strongest red fluorescence, indicating a higher MMP. Cells treated with CUR/HCA showed strong green fluorescence, suggesting a lower MMP. Cells treated with CUR/HCA and exposed to laser light displayed the most intense green fluorescence, indicating severe mitochondrial damage exacerbated by laser exposure.

Since mitochondria are the main source of ATP generation, any mitochondrial damage has the potential to cause a reduction in ATP levels. We used an ATP content detection kit to measure intracellular ATP levels after incubation with various treatments (Fig. 4D and S9). In comparison to the control group, no noteworthy alterations in ATP content in the CUR-only or HCA-only groups, suggesting that free CUR or the presence of free Ca^{2+} alone did not cause significant mitochondrial damage. However, the ATP content in cells treated with CUR/HCA was significantly reduced, indicating that the simultaneous presence of CUR and free Ca^{2+} effectively induced mitochondrial damage, resulting in decreased ATP production.

3.9. *In vitro* cytotoxicity caused by calcium overload photothermal

As shown in Fig. 4E, a standard Alamar Blue assay was conducted to assess the inhibition of cell proliferation *in vitro*. Compared to the control group, all experimental groups demonstrated various levels of cytotoxicity, with a corresponding decrease in cell viability as the CUR concentration escalated. Moreover, laser irradiation also hindered the growth of cancer cells by elevating the

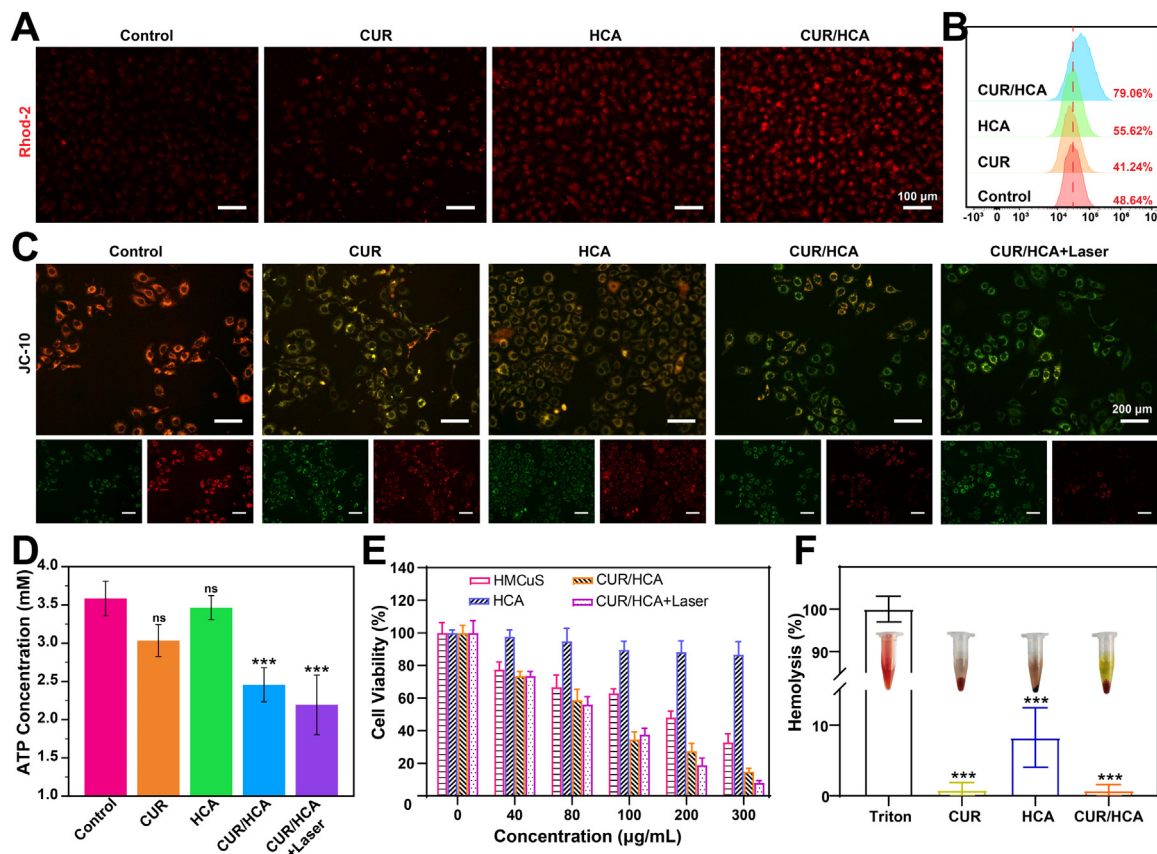


Fig. 4 – CLSM images of intracellular Ca^{2+} distribution and mitochondrial damage. (A) Fluorescence image of HeLa cells treated with various materials (red: Ca^{2+} ; Scale bar: 100 μm). (B) Quantification of calcium ion fluorescence intensity in HeLa cells by flow cytometry. (C) MMP changes of HeLa cells treated with different preparations by fluorescence microscope (green: polymer, red: monomer. Scale bar: 200 μm). (D) ATP production after co incubation with various materials ($n = 3$). (E) Cell inhibition rates for different treatments on HeLa cells for 24 h ($n = 5$). (F) Blood compatibility of CUR, HCA and CUR/HCA ($n = 5$; * $P < 0.05$, ** $P < 0.01$, * $P < 0.001$).**

temperature. Notably, the combined application of CUR/HCA and laser therapy exhibited a significantly stronger inhibitory impact on cancer cell viability. To illustrate, at a material concentration of 200 $\mu\text{g}/\text{ml}$, the HCA group resulted in roughly 11.78% cell death, whereas CUR/HCA led to 72.58% cell death, leaving only 18.94% of cells viable after laser treatment. This notable effect is primarily attributed to the synergistic action of calcium overload and photothermal therapy, highlighting the immense therapeutic potential of our developed material for tumor treatment. Additionally, our observations indicate that HMCuS displays inherent cytotoxicity even in the absence of illumination. This could be attributed to its Fenton-like catalytic activity and its ability to disrupt copper homeostasis, specifically through the degradation of Cu^{2+} and Cu^+ ions [41,45]. Furthermore, the hemolysis experiment provided additional evidence of the remarkable biocompatibility of our prepared material, as depicted in Fig. 4F. All experimental groups exhibited significantly reduced hemolysis rates when compared to the positive control. Impressively, the CUR/HCA group demonstrated an exceptionally low hemolysis rate of merely 0.74%.

3.10. Transcriptome analysis of HeLa cells after treating with CUR/HCA

To further investigate the mechanism behind cascade-enhanced calcium overload on tumor cell apoptosis, the RNA sequencing on HeLa cells exposed to different materials were conducted. Unsupervised hierarchical clustering analysis showed that sample data from identical treatment groups clustered tightly, underscoring the high quality of our RNA sequencing results (Fig. 5A and S9A). We proceeded to examine the differentially expressed genes (DEGs) across groups, noting a substantial number of DEGs when contrasting the treatment and control groups. This finding indicates that each treatment had a unique impact on HeLa cells (Fig. S10B). Our main focus was on the DEGs between the CUR/HCA-treated group and the control group. The results, summarized in Fig. 5B, reveal a total of 2,866 DEGs between these two groups, with 2,628 genes upregulated and 238 genes downregulated. One noteworthy observation was the downregulation of the FOS gene in the CUR/HCA+Laser group compared to the CUR/HCA group alone (Fig. S10C). Prior

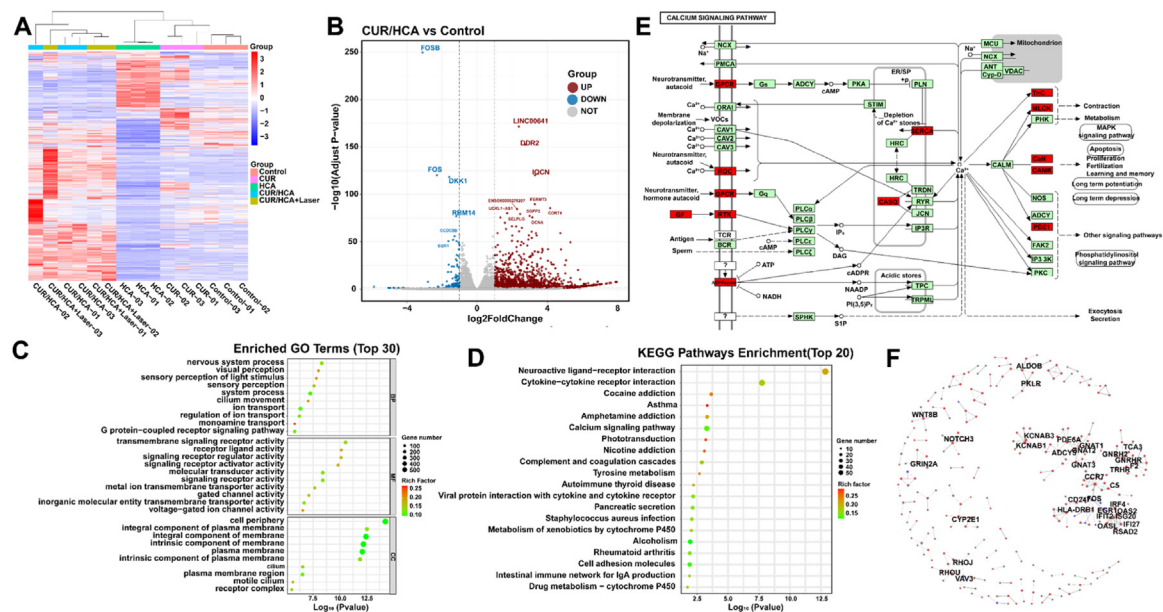


Fig. 5 – RNA-seq analysis of DEGs between PBS and CUR/HCA. (A) Heatmap of DEGs between PBS, CUR, HCA, CUR/HCA and CUR/HCA+Laser. **(B)** Volcano plot of DEGs between CUR/HCA and PBS. **(C)** GO enrichment analysis of DEGs between CUR/HCA and PBS. **(D)** KEGG enrichment analysis of DEGs between CUR/HCA and PBS. **(E)** Calcium signaling pathway analysis of DEGs between CUR/HCA and PBS (Light green background: genes present in the KEGG pathway; Red background: upregulated DEGs; Green background: downregulated DEGs). **(F)** PPI network analysis of DEGs between CUR/HCA and PBS.

research has established a strong correlation between FOS gene expression and tumorigenesis [46]. Our finding suggests that CUR/HCA, when combined with laser irradiation, can significantly decrease the expression of the FOS gene, thereby potentially inhibiting tumor formation.

The top 30 genes, with absolute correlation coefficients exceeding 0.95, were rigorously selected and underwent gene ontology (GO) enrichment analysis. Fig. 5C illustrates that the DEGs linked to CUR/HCA treatment are predominantly enriched in molecular functions such as 'receptor and ligand activity', 'transmembrane signaling' and 'metal ion and cation channel activity'. These DEGs also show higher expression in cellular components including 'cell membranes' and 'plasma membranes' and 'ion channel complexes'. This suggests that the nano-vehicles we've developed significantly affect ligand-receptor interactions and ion channel activities. Moreover, it hints that CUR/HCA is transported into cells via transmembrane processes.

To exploit the cascade enhancement mechanism, GO enrichment analyses were conducted on the upregulated DEGs between CUR/HCA and CUR (Fig. S10D) and between CUR/HCA and HCA (Fig. S10E). Remarkably, in comparison to CUR and HCA, the upregulated DEGs of CUR/HCA exhibited significant enrichment in functions related to signaling receptors and transmembrane transporters. Specifically, the DEGs of CUR/HCA versus CUR notably influenced 'channel activity', while the DEGs of CUR/HCA compared to HCA affected 'calcium ion binding'. These results imply that the combined presence of CUR and exogenous Ca^{2+} has a profound effect on the calcium signaling pathway, ultimately leading to amplified calcium overload.

In addition, the Kyoto Encyclopedia of Genes and Genomes (KEGG) pathway analysis was conducted to assess biological responses after CUR/HCA treatment (Fig. 5D). The KEGG enrichment results verified that the DEGs were primarily associated with pathways including 'neuronal ligand receptor interaction', 'cocaine and amphetamine addiction', and the 'calcium ion signaling pathway'. Alterations in signaling pathways linked to cocaine and amphetamine addiction can be traced back to modifications in calcium ion pathways. This is because neuroconduction activity and synaptic transmission have been demonstrated to have a close correlation with ion channels, as evidenced in previous studies [47,48]. These findings implicate that the nano-vehicles we've developed impact the calcium ion signaling pathways, subsequently influencing nerve conduction and potentially inducing cell apoptosis.

To illustrate the layout of DEGs within the pathway, annotations were made in the calcium signaling pathway diagram (Fig. 5E). Numerous genes within the calcium signaling pathway are upregulated in HeLa cells treated with CUR/HCA, significantly disrupting intracellular Ca^{2+} homeostasis. As depicted in Fig. 5F, a protein-protein interaction (PPI) network analysis was conducted on the DEGs. These DEGs are primarily associated with proteins involved in tumor proliferation and differentiation, such as FOS, CXCL8 and ERG1. Additionally, they are linked to proteins like IFI27 that influence mitochondrial metabolism. Collectively, these findings suggest that CUR/HCA induces mitochondrial calcium overload by modulating calcium ion channels, thereby affecting mitochondrial metabolic functions and ultimately leading to cell apoptosis. However,

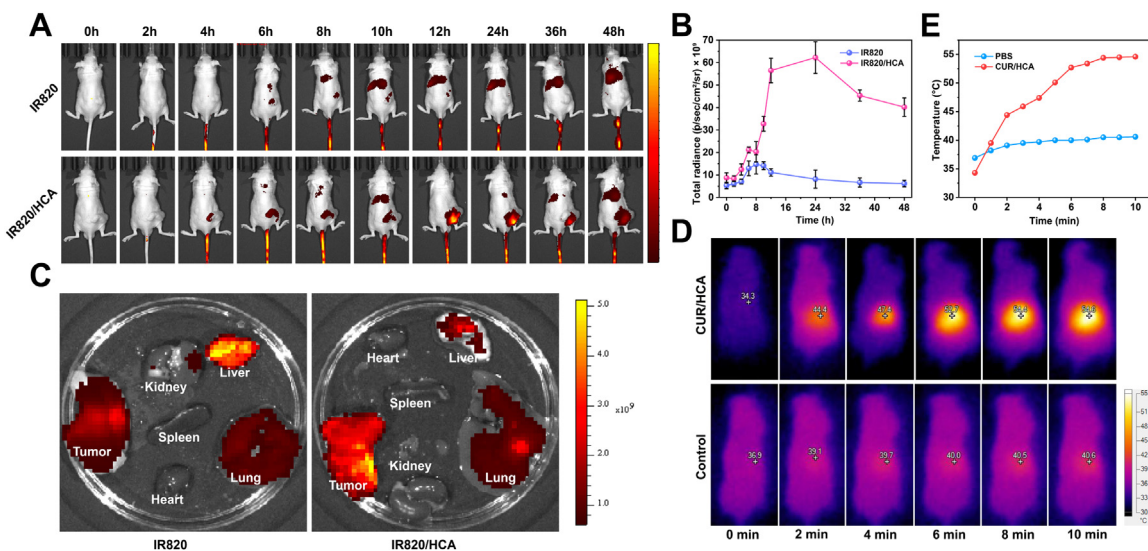


Fig. 6 – In vivo biodistribution and photothermal of calcium-based nanovehicles. (A) In vivo fluorescent images of tumor-bearing mice at different times after injection with IR820 and IR820/HCA in a vein. **(B)** Quantify IR820 fluorescence intensity in tumors. **(C)** In vitro fluorescent imaging of tissues at 48 h post-injection. **(D)** Thermal images of mice treated by PBS and CUR/HCA for different time (NIR: 1,064 nm laser, power: 1 W/cm², time: 10 min). **(E)** Heating curve in tumors.

further investigation is warranted to explore the protein expression associated with calcium overload-induced cell apoptosis channels.

3.11. In vivo biodistribution of CUR/HCA

IR820-labeled HCA was used to visualize the distribution of nanovehicles in vivo. As depicted in Fig. 6A, within 12-h injecting the drug into the tail vein, fluorescence signals were predominantly detected in the liver and tail region. This observation can be explained by the limited biocompatibility of IR820 and its inability to circulate freely throughout the body via the bloodstream. In contrast, for the IR820/HCA group, fluorescence signals gradually accumulated from the tail to the tumor site over time, peaking at 12 h post-injection (Fig. 6B). In vitro fluorescence imaging provided further insights into the distribution of IR820 and IR820/HCA within the vital organs of tumor-bearing mice (Fig. 6C). Notably, minimal fluorescence signals were detected in the tumors of the IR820 group, with most signals concentrated in the liver. Conversely, the tumors in the IR820/HCA group exhibited the strongest fluorescence signals. The in vivo and in vitro distribution patterns of IR820/HCA demonstrate that HCA can effectively accumulate at tumor sites, highlighting its remarkable potential as a multifunctional nanovehicle for targeted tumor therapy.

3.12. In vivo photothermal effect of CUR/HCA

To visually assess the impact of photothermal therapy, an in vivo evaluation of the photothermal effect was performed after injecting PBS or CUR/HCA via the tail vein. As shown in Fig. 6D and 6E, the temperature of the tumor-bearing mice injected with CUR/HCA rose to 54.6 °C within 10 min under 1064 nm laser irradiation. In comparison, the control

group only achieved a temperature increase to 40.6 °C. This significant temperature difference underscores the efficient photothermal heating capability of CUR/HCA in vivo.

3.13. Antitumor effect of CUR/HCA

To further investigate the impact of CUR/HCA on tumor growth inhibition, the in vivo anti-tumor experiments were carried out, as summarized in Fig. 7A. The results revealed distinct effects on tumor growth depending on the materials injected via the tail vein. Specifically, the CUR/HCA group demonstrated a more pronounced ability to restrain tumor proliferation compared to the HCA and CUR groups. This underscores that effective calcium overloading relies on the simultaneous presence of exogenous Ca²⁺ and CUR. Notably, tumor volume was significantly reduced after laser irradiation, indicating that the nanovehicles can collaboratively eliminate tumor cells through a cascade-enhanced calcium overloading mechanism (Fig. 7B). Throughout three rounds of treatment with various preparations, no significant changes were observed in the body weight of the mice, suggesting that the nanovehicles were well-tolerated without apparent side effects (Fig. 7C). Images of dissected mouse tumors 13 d post-treatment further support the efficacy of cascade-enhanced calcium overloading in cancer cell elimination (Fig. 7D and S11). The corresponding tumor weights are documented in Fig. 7E. Mice treated with CUR/HCA, particularly those that also received laser treatment, exhibited lighter tumor weights. This suggests that the triple action of CUR, exogenous Ca²⁺ and laser irradiation achieves a cascade-enhanced calcium overloading, resulting in a more pronounced inhibitory effect on tumors.

To provide a more detailed visualization of the damage inflicted on cancerous cells within the tumor, we performed

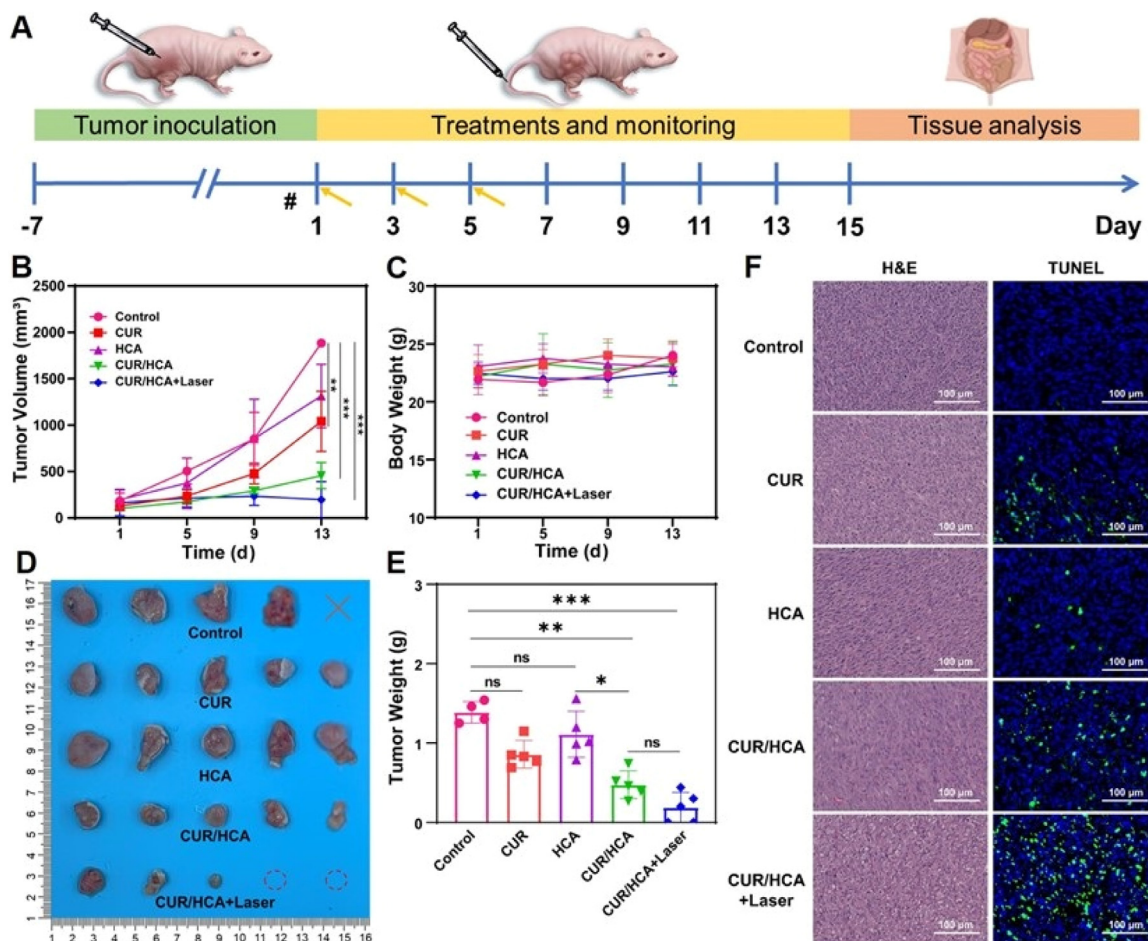


Fig. 7 – Anticancer effects in vivo. (A) Treatment schedule in vivo. # The time pointed to by the arrow represents the time of tail vein injection. (B) Tumor growth curves of tumor-bearing mice after treatment with various materials. (C) Body weight changes of tumor-bearing mice after treatment with various materials. (D) Tumor picture of tumor-bearing mice at the end of treatment. # 'o' represent tumor disappearance and 'x' represents accidental death of the mouse. (E) Tumor weight changes of tumor-bearing mice after treatment with various materials. (F) H&E-stained and TUNEL-stained tumor biopsies collected from tumor-bearing mice at the end of treatment. Data are presented as mean ± SD ($n = 5$; * $P < 0.05$, ** $P < 0.01$, *** $P < 0.001$).

H&E staining and TUNEL staining on tumor tissue samples. The results showed a significant decrease in cancerous cells in the tumor tissue sections from mice treated with CUR/HCA. Notably, the lowest number of cancerous cells was observed in the group that underwent laser treatment, corroborating the findings from our in vivo treatment studies (Fig. 7F). Additionally, H&E staining of normal tissue (Fig. S12) revealed no significant differences between the treatment group and the control group, suggesting that the prepared nanovehicles did not cause any apparent side effects on normal tissues.

4. Conclusion

In this study, we have successfully developed a nano-delivery platform that leverages a cascade effect to amplify calcium overloading for cancer therapy. The CUR/HCA

nanoparticles rapidly degrade in the TME, releasing a considerable amount of exogenous Ca^{2+} . This process is augmented by the synergistic action of CUR, which disrupts mitochondrial calcium homeostasis. Importantly, the photothermal properties of CUR/HCA not only facilitate the degradation of amorphous ACC, boosting the release of exogenous Ca^{2+} , but also enhance calcium overload to eliminate cancer cells. Transcriptome analysis reveals that CUR/HCA modulates calcium homeostasis by upregulating genes involved in the calcium signaling pathway, ultimately inducing calcium overload. Comprehensive in vivo and in vitro studies demonstrate that CUR/HCA can evade lysosomal sequestration, accumulate at tumor sites, and potently inhibit cancer cell proliferation through a cascade-enhanced calcium overloading approach, synergistically with photothermal therapy. We believe that this nanoplatform represents a highly promising therapeutic strategy for the treatment of cervical cancer via calcium overloading.

Conflicts of interest

The authors report no conflicts of interest. The authors are responsible for the content and writing of this article.

Acknowledgments

This research was sponsored by the key research program of Ningbo (No. 2023Z210), funded by Ningbo Natural Science Foundation (No. 202003N4006) and the Joint Research Funds of Department of Science & Technology of Shaanxi Province, Northwestern Polytechnical University (No. 2020GXZH-Z-017).

Supplementary materials

Supplementary material associated with this article can be found, in the online version, at doi:10.1016/j.ajps.2024.100989. The figures with "S" before the serial number are included in the Supplementary material.

REFERENCES

- [1] Siegel RL, Miller KD, Wagle NS, Jemal A. Cancer statistics, 2023. CA Cancer J Clin 2023;73(1):17–48.
- [2] Miller KD, Nogueira L, Devasia T, Mariotto AB, Yabroff KR, Jemal A, et al. Cancer treatment and survivorship statistics. CA Cancer J Clin 2022;72(5):409–36.
- [3] Sung H, Ferlay J, Siegel RL, Laversanne M, Soerjomataram I, Jemal A, et al. Global cancer statistics 2020: GLOBOCAN estimates of incidence and mortality worldwide for 36 cancers in 185 countries. CA Cancer J Clin 2021;71(3):209–49.
- [4] Xia C, Dong X, Li H, Cao M, Sun D, He S, et al. Cancer statistics in China and United States, 2022: profiles, trends, and determinants. Chin Med J 2022;135(5):584–90.
- [5] Small W Jr, Bacon MA, Bajaj A, Chuang LT, Fisher BJ, Harkenrider MM, et al. Cervical cancer: a global health crisis. Cancer 2017;123(13):2404–12.
- [6] Koh WJ, Abu-Rustum NR, Bean S, Bradley K, Campos SM, Cho KR, et al. Cervical cancer, version 3.2019, NCCN clinical practice guidelines in oncology. J Natl Compr Canc Netw 2019;17(1):64–84.
- [7] Friedman JR, Nunnari J. Mitochondrial form and function. Nature 2014;505(7483):335–43.
- [8] Chandel NS. Mitochondria as signaling organelles. BMC Biol 2014;12:34.
- [9] Pathak T, Trebak M. Mitochondrial Ca^{2+} signaling. Pharmacol Ther 2018;192:112–23.
- [10] Vasan K, Werner M, Chandel NS. Mitochondrial metabolism as a target for cancer therapy. Cell Metab 2020;32(3):341–52.
- [11] Vyas S, Zaganjor E, Haigis MC. Mitochondria and cancer. Cell 2016;166(3):555–66.
- [12] Lu J, Song L, Feng S, Wang K, Mao Y, Gao Y, et al. Nanozyme-mediated biocatalysis as a mitochondrial oxidative stress amplifier for tumor nanocatalytic immunotherapy. Chem Eng J 2024;481:148270.
- [13] Feng S, Xiao Y, Lu J, Chen Z, Jiang Z, Xu Q, et al. Tumor microenvironment sensitization via dual-catalysis of carbon-based nanoenzyme for enhanced photodynamic therapy. J Colloid Interface Sci 2024;663:577–90.
- [14] Marchi S, Paternani S, Missiroli S, Morciano G, Rimessi A, Wieckowski MR, et al. Mitochondrial and endoplasmic reticulum calcium homeostasis and cell death. Cell Calcium 2018;69:62–72.
- [15] Vakifahmetoglu-Norberg H, Ouchida AT, Norberg E. The role of mitochondria in Metabolism and Cell Death. Biochem Biophys Res Commun 2017;482(3):426–31.
- [16] Sabharwal SS, Schumacker PT. Mitochondrial ROS in cancer: initiators, amplifiers or an achilles' heel? Nat Rev Cancer 2014;14(11):709–21.
- [17] Paillusson S, Gomez-Suaga P, Stoica R, Little D, Gissen P, Devine MJ, et al. Alpha-synuclein binds to the ER-mitochondria tethering protein VAPB to disrupt Ca^{2+} homeostasis and mitochondrial ATP production. Acta Neuropathol 2017;134(1):129–49.
- [18] Srinivasan S, Guha M, Kashina A, Avadhani NG. Mitochondrial dysfunction and mitochondrial dynamics—the cancer connection. Biochim Biophys Acta Bioenerg 2017;1858(8):602–14.
- [19] Shao F, Han J, Tian Z, Wang Z, Liu S, Wu Y. Synergistic ROS generation and directional overloading of endogenous calcium induce mitochondrial dysfunction in living cells. Biomaterials 2023;301:122284.
- [20] Pesakhov S, Nachliely M, Barvatz Z, Aqaqe N, Schwartzman B, Voronov E, et al. Cancer-selective cytotoxic Ca^{2+} overload in acute myeloid leukemia cells and attenuation of disease progression in mice by synergistically acting polyphenols curcumin and carnosic acid. Oncotarget 2016;7(22):31847–31861.
- [21] Sun Y, Chen YY, Ma XY, Yuan Y, Liu CS, Kohn J, et al. Mitochondria-targeted hydroxyapatite nanoparticles for selective growth inhibition of lung cancer in vitro and in vivo. ACS Appl Mater Interfaces 2016;8(39):25680–90.
- [22] Zhou Q, Xiang J, Qiu N, Wang Y, Piao Y, Shao S, et al. Tumor abnormality-oriented nanomedicine design. Chem Rev 2023;123(18):10920–89.
- [23] Liu X, Qi M, Li X, Wang J, Wang M. Curcumin: a natural organic component that plays a multi-faceted role in ovarian cancer. J Ovarian Res 2023;16(1):47.
- [24] Xu X, Chen D, Ye B, Zhong F, Chen G. Curcumin induces the apoptosis of non-small cell lung cancer cells through a calcium signaling pathway. Int J Mol Med 2015;35(6):1610–16.
- [25] Ma Z, Wang N, He H, Tang X. Pharmaceutical strategies of improving oral systemic bioavailability of curcumin for clinical application. J Control Release 2019;316:359–80.
- [26] Chen J, Qiu M, Zhang S, Li B, Li D, Huang X, et al. A calcium phosphate drug carrier loading with 5-fluorouracil achieving a synergistic effect for pancreatic cancer therapy. J Colloid Interface Sci 2022;605:263–73.
- [27] Yan J, Ma X, Liang D, Ran M, Zheng D, Chen X, et al. An autocatalytic multicomponent DNAzyme nanomachine for tumor-specific photothermal therapy sensitization in pancreatic cancer. Nat Commun 2023;14(1):6905.
- [28] Zhang M, Song R, Liu Y, Yi Z, Meng X, Zhang J, et al. Calcium-overload-mediated tumor therapy by calcium peroxide nanoparticles. Chem 2019;5(8):2171–82.
- [29] Zheng P, Ding B, Shi R, Jiang Z, Xu W, Li G, et al. A Multichannel Ca^{2+} nanomodulator for multilevel mitochondrial destruction-mediated cancer therapy. Adv Mater 2021;33(15):e2007426.
- [30] Zheng P, Ding B, Jiang Z, Xu W, Li G, Ding J, et al. Ultrasound-augmented mitochondrial calcium ion overload by calcium nanomodulator to induce immunogenic cell death. Nano Lett. 2021;21(5):2088–93.
- [31] Zheng P, Ding B, Zhu G, Li C, Lin J. Biodegradable Ca^{2+} Nanomodulators activate pyroptosis through mitochondrial Ca^{2+} overload for cancer immunotherapy. Angew Chem Int Ed 2022;61(36):e202204904.
- [32] Xue CC, Li MH, Zhao Y, Zhou J, Hu Y, Cai KY, et al. Tumor microenvironment-activatable Fe-doxorubicin preloaded

- amorphous CaCO_3 nanoformulation triggers ferroptosis in target tumor cells. *Sci Adv* 2020;6(18):eaax1346.
- [33] Dong Z, Feng L, Hao Y, Chen M, Gao M, Chao Y, et al. Synthesis of hollow biomimetic CaCO_3 -polydopamine nanoparticles for multimodal imaging-guided cancer photodynamic therapy with reduced skin photosensitivity. *J Am Chem Soc* 2018;140(6):2165–78.
- [34] Wang C, Yu F, Liu X, Chen S, Wu R, Zhao R, et al. Cancer-specific therapy by artificial modulation of intracellular calcium concentration. *Adv Healthc Mater* 2019;8(18):e1900501.
- [35] Zhang Y, Feng X, Jia X, Zhao J, Hao Y, Wang H, et al. Biomimetic Ca^{2+} nanogenerator based on ions interference strategy for tumour-specific therapy. *J Drug Target* 2021;29(10):1094–101.
- [36] Ma X, Wang P, Wu Q, Zhou J, Wang D, Yadav D, et al. Porphyrin centered paclitaxel tetrameric prodrug nanoassemblies as tumor-selective theranostics for synergized breast cancer therapy. *Adv Healthc Mater* 2023;12(2):2202024.
- [37] Xiao Y, Li Z, Bianco A, Ma B. Recent advances in calcium-Based anticancer nanomaterials exploiting calcium overload to trigger cell apoptosis. *Adv Funct Mater* 2022;33(3):2209291.
- [38] Xu L, Tong G, Song Q, Zhu C, Zhang H, Shi J, et al. Enhanced intracellular Ca^{2+} nanogenerator for tumor-specific synergistic therapy via disruption of mitochondrial Ca^{2+} homeostasis and photothermal therapy. *ACS Nano* 2018;12(7):6806–18.
- [39] Lu J, Wang W, Xu Z, Zhang P, Gu J, Xu Z, et al. CaCO₃-Assistant synthesis of pH/near-infrared light-responsive and injectable sodium alginate hydrogels for melanoma synergistic treatment. *J Colloid Interface Sci* 2023;633:657–67.
- [40] Wang S, Riedinger A, Li H, Fu C, Liu H, Li L, et al. Plasmonic copper sulfide nanocrystals exhibiting near-infrared photothermal and photodynamic therapeutic effects. *ACS Nano* 2015;9(2):1788–800.
- [41] Liu X, Geng P, Yu N, Xie Z, Feng Y, Jiang Q, et al. Multifunctional doxorubicin@hollow- Cu_9S_8 nanoplatforms for photothermally-augmented chemodynamic-chemo therapy. *J Colloid Interface Sci* 2022;615:38–49.
- [42] Deng X, Li K, Cai X, Liu B, Wei Y, Deng K, et al. A hollow-structured $\text{CuS}@\text{Cu}_2\text{S}@\text{Au}$ nanohybrid: synergistically enhanced photothermal efficiency and photoswitchable targeting effect for cancer theranostics. *Adv Mater* 2017;29(36):1701266.
- [43] Ding D, Mei Z, Huang H, Feng W, Chen L, Chen Y, et al. Oxygen-independent sulfate radical for stimuli-responsive tumor nanotherapy. *Adv Sci* 2022;9(17):e2200974.
- [44] Li Z, Gan B, Li Z, Zhang H, Wang D, Zhang Y, et al. Kinetic mechanisms of methane hydrate replacement and carbon dioxide hydrate reorganization. *Chem Eng J* 2023;477(1):146973.
- [45] Xue Q, Kang R, Klionsky DJ, Tang D, Liu J, Chen X. Copper metabolism in cell death and autophagy. *Autophagy* 2023;19(8):2175–95.
- [46] Zhu YT, Hu L, Qi C, Zhu YJ. PRIP Promotes tumor formation through enhancing serum-responsive factor-mediated FOS expression. *J Biol Chem* 2009;284(21):14485–92.
- [47] Wang Y, Yang L, Zhou H, Zhang K, Zhao M. Identification of miRNA-mediated gene regulatory networks in L-methionine exposure counteracts cocaine-conditioned place preference in mice. *Front Genet* 2023;13:1076156.
- [48] Lambert MO, Ipsen TH, Kohlmeier KA. Acute cocaine exposure elicits rises in calcium in arousal-related laterodorsal tegmental neurons. *Pharmacol Res Perspect* 2017;5(1):e00282.